J Adv Ceram 2026, **15**: 9221297
https://doi.org/10.26599/JAC.2026.9221297
Research Article

Enhancing densification and mechanical performance of B_4C ceramics using $Y_3Si_2C_2$ as a novel sintering additive

Lirui He[1,2], Pengxing Cui[2], Gang Qin[2], Bin Wang[1,2], Tiantian Tao[1,2], Xiaobing Zhou[1,2,✉]

[1] *School of Materials Science and Chemical Engineering, Ningbo University, Ningbo 315211, China*

[2] *Zhejiang Key Laboratory of Data-Driven High-Safety Energy Materials and Applications, Ningbo Key Laboratory of Special Energy Materials and Chemistry, Ningbo Institute of Materials Technology and Engineering, Chinese Academy of Sciences, Ningbo 315201, China*

✉ Corresponding author.

E-mail: zhouxb@nimte.ac.cn

Received: January 28, 2026; Revised: March 24, 2026; Accepted: April 11, 2026

Abstract: Boron carbide (B_4C) is a highly strong covalent ceramic material with a low surface diffusion coefficient, making it extremely difficult to consolidate at low temperature. Therefore, the development of effective sintering additives that enable low-temperature, high-density consolidation, while maintaining excellent mechanical

properties, remains a critical challenge for scalable application of B_4C. In this study, $Y_3Si_2C_2$ was employed as a novel sintering additive to enhance the densification and mechanical performance of B_4C ceramics, for the first time. B_4C ceramics containing 0-10 wt.% $Y_3Si_2C_2$ were fabricated using spark plasma sintering (SPS) technique at temperature ranging from 1700 °C to 1900 °C. The effects of $Y_3Si_2C_2$ sintering additive content and sintering temperature on the densification behavior, microstructure, and mechanical properties of the B_4C ceramics were systematically investigated. The results indicate that $Y_3Si_2C_2$ facilitates the densification of B_4C ceramics via an in-situ reactive liquid-phase sintering mechanism. The formation of Y-rich liquid phase significantly enhances particle rearrangement and mass transport, while the in-situ generated YB_4 phase pins grain boundaries and suppress abnormal grain growth. As a result, the mechanical properties of the B_4C ceramics were significantly improved. Optimal comprehensive mechanical properties were achieved at 1800 °C with 8 wt.% $Y_3Si_2C_2$, yielding a Vickers hardness of 31.4 GPa, and a flexural strength of 694.0 MPa. This work paves the way for rare earth silicon carbide as a novel sintering additive of B_4C ceramics to enhance the densification and mechanical performance for extreme environment applications.

Keywords: B_4C, $Y_3Si_2C_2$, spark plasma sintering, sintering additives

1 Introduction

Boron carbide (B_4C) is a highly promising engineering material characterized by high hardness (>30 GPa), low density (2.52 $g \cdot cm^{-3}$), and a high melting point (2450 °C) [1, 2]. B_4C is widely used in abrasives and grinding media, as well as in the fabrication of lightweight, high-strength military components such as body armor, ballistic inserts, and armor plates [3-5]. Owing to its large neutron absorption cross-section, B_4C also serves as an effective absorber and shielding material for advanced nuclear reactors [6-8]. However, B_4C is a strong covalent ceramic with high covalent B-B and B-C bonds result in a low self-diffusion coefficient, sluggish grain boundary migration, and a correspondingly high sintering temperature requirement [9, 10]. Furthermore, excellent mechanical properties are a prerequisite for the engineering application of B_4C ceramics. Therefore, simultaneously lowering the sintering temperature while improving the mechanical properties remains a key challenge to expanding the practical application value of B_4C ceramics.

Currently, pressure-assisted sintering techniques and/or the addition of sintering additives are widely employed to enhance the densification and mechanical properties of B_4C ceramics. Spark Plasma Sintering (SPS) is an advanced sintering technique that combines uniaxial pressure with high-intensity pulsed direct current [11]. It enables rapid densification of bulk materials via the Joule heating effect and has been extensively employed in the fabrication of boron carbide ceramics [12-15]. Grippi et al [15]. investigated the influence of sintering parameters on the relative density and

microstructure of additive-free B_4C ceramics. They achieved a density of 2.06 $g \cdot m^{-3}$ and a relative density of 81.7% at 1800 °C under an applied pressure of 60 MPa. Moshtaghioun et al. [16] fabricated monolithic B_4C ceramics by SPS using B_4C starting powder with an average particle size of 500 nm. Under sintering conditions of 1800 °C and 75 MPa, B_4C ceramics with a relative density of 99.2%, a Vickers hardness (HV_2) of 29 ± 2 GPa, and a fracture toughness of 2.0 ± 0.1 $MPa \cdot m^{1/2}$ were successfully achieved.

Although SPS technology can produce relatively dense B_4C ceramics, the densification of pure B_4C generally requires relatively severe conditions, including high temperatures and large applied pressures. The introduction of sintering additives not only lowers the required sintering temperature, but can also significantly enhance the mechanical properties of the material [17, 18]. Commonly used sintering additives for B_4C ceramics include nonmetallic elements (C [19], Si [20]), metallic elements (Al [21], Fe [22]), metal oxides (ZrO_2 [23], Y_2O_3 [24], La_2O_3 [25]), silicides ($ZrSi_2$ [26]), carbides (SiC [27]), and borides (TiB_2 [28]). According to their sintering mechanisms, these additives can be categorized as liquid-phase or solid-state sintering aids. While liquid-phase additives are effective in reducing sintering temperature and refining the grain structure, residual intergranular phases may adversely affect hardness. In contrast, B_4C ceramics prepared via solid-state sintering typically exhibit superior intrinsic properties, but are susceptible to strength degradation due to grain coarsening [29]. Therefore, a combined strategy incorporating both liquid-phase and solid-state sintering effects is

considered optimal for achieving high-performance B_4C ceramics.

$Y_3Si_2C_2$ (yttrium silicon carbide) is a typical rare-earth silicon carbide ($RE_3Si_2C_2$), characterized by a unique layered structure and a relatively low melting point of approximately 1590 °C, which is below the conventional sintering temperature of B_4C ceramics [30-32]. This enables the formation of a liquid phase during sintering, thereby facilitating atomic diffusion and enhancing densification. Furthermore, $Y_3Si_2C_2$ exhibits a strong affinity for oxygen, which facilitates the removal of surface oxide layers on B_4C particle, thereby improving interparticle contact and accelerating mass transport. Owing to these advantages, $Y_3Si_2C_2$ has been successfully used in the sintering of various covalently bonded ceramics, such as SiC [33] and Si_3N_4 [30]. In addition, at elevated temperatures, $Y_3Si_2C_2$ could react with the B_4C matrix to form carbides as well as borides and reinforced phases, contributing to enhanced mechanical properties. Nevertheless, despite these promising characteristics, the application of $Y_3Si_2C_2$ in B_4C ceramics remains largely unexplored.

In the present study, dense B_4C ceramics were prepared by spark plasma sintering. The effects of $Y_3Si_2C_2$ content and sintering temperature on phase composition and microstructure evolution of B_4C ceramics were systematically investigated, and their influence on mechanical and thermoelectric properties was analyzed. In addition, the liquid-phase sintering mechanisms associated with $Y_3Si_2C_2$ were elucidated, together with the in-situ reaction products formed during the sintering process.

2 Experimental procedures

B_4C powder (99%, D_{50} = 0.97 μm, Xuancheng Jingrui New Materials Co., Ltd., China), YH_2 powder (99.5%, average particle size 75.0 μm, Hunan Institute of Rare-Earth Metals, China), β-SiC powder (99.5%, average particle size 0.5 μm, Qinhuangdao Yinuo Advanced Materials, China), and $Y_3Si_2C_2$ (D_{50} = 1.96 μm, homemade) were used as raw materials for the experiments.

$Y_3Si_2C_2$ sintering additive was synthesized via solid-state reaction in our lab. YH_2 and β-SiC were mixed in a stoichiometric ratio, placed in a vacuum graphite furnace, and sintered at 1300 °C for 5 hours under an argon atmosphere. After grinding in a planetary ball mill for 8 hours, $Y_3Si_2C_2$ powder with an average particle size of 1.956 μm was obtained. B_4C and $Y_3Si_2C_2$ powders were wet-blended at ratios of X wt.% $Y_3Si_2C_2/B_4C$ (X = 0, 2, 4, 6, 8, 10). The blended powders were mixed for 4 hours using ethanol as the dispersing medium and silicon carbide balls as the milling media. The dried powder mixture was sieved through a 200-mesh screen and subsequently loaded into graphite crucibles with a diameter of 20 mm. Sintering was carried out at 1700 °C using an HPD25 spark plasma sintering (SPS) system (FCT GmbH, Germany). The heating/cooling rate was 50 °C/min, with a dwell time of 30 min at 1700 °C under an applied pressure of 50 MPa. The samples produced at this temperature were denoted as 17-X, where X represents the $Y_3Si_2C_2$ additive content (0, 2, 4, 6, 8, 10 wt.%). For the samples containing 8 wt.% additive, additional sintering experiments were conducted at temperatures of 1800 °C and 1900 °C, resulting in samples designated as 18-8 and

19-8, respectively. Under otherwise identical processing conditions, B_4C powder was also consolidated in a graphite die with an inner diameter of 42 mm using SPS. The sintered bodies were subsequently ground and cut into rectangular bars with dimensions of 3 × 4 × 30 mm^3 for three-point bending tests. In addition, to understand the in-situ reaction proccess among B_4C and $Y_3Si_2C_2$ as well as the possible oxides, such as Y_2O_3, SiO_2, and B_2O_3, the 10 wt.% $Y_3Si_2C_2/B_4C$ powder was sintered at temperatures ranging from 800 to 1600 °C with heating/cooling rate of 50 °C/min, while without dwelling time under an applied pressure of 50 MPa.

The apparent density of the samples was measured using the Archimedes method. Phase analysis of the starting powders and B_4C ceramics was performed by X-ray diffraction (XRD, D8 Advance, Bruker AXS, Germany). Microstructural characterisation was carried out using scanning electron microscopy (SEM, Regulus 8230, Hitachi, Japan). Further phase identification was performed by transmission electron microscopy (TEM, Talos F200x, Thermo Fisher Scientific, USA) on thin lamellae prepared by focused ion beam milling (FIB, Auriga, Carl Zeiss, USA). Prior to microscopic observation, the specimens were electrochemically etched in a 2 $mol \cdot L^{-1}$ KOH solution at an applied voltage of 0.3 V. Statistical grain size analysis was conducted by measuring at least 100 grains from SEM images using Nanomeasure software.

Thermal diffusivity (α) and specific heat capacity (C_p) at room temperature were measured using a laser flash apparatus (LFA467, Netzsch-Gerätebau GmbH, Germany).

The thermal conductivity (k) was subsequently calculated according to $k = \alpha \cdot \rho \cdot C_p$, where ρ is the measured apparent density. Electrical resistivity was determined using a four-point probe system (Model 280DI, Four Dimensions, USA), and the corresponding electrical conductivity was obtained as the reciprocal of the resistivity.

Vickers hardness was measured using an automatic hardness tester (Buehler Wilson VH3300, USA) under an applied load of 20 N with a dwell time of 10 s. Mechanical testing of rectangular samples ($3 \times 4 \times 30$ mm^3) was conducted using a universal testing machine (Zwick Roell Z250AF) with a span of 20 mm and a crosshead speed of 0.5 mm/min.

3 Results and discussion

3.1 Microstructure and phase composition of powders

Fig. 1 shows the XRD patterns and microstructural features of the B_4C powder, the as-synthesized $Y_3Si_2C_2$ powder, and their mixed powder. The major diffraction peaks of the raw B_4C powder are consistent with the standard PDF card (#00-035-0798, B_4C). An additional peak observed at $2\theta \approx 28°$ corresponds to boric acid (H_3BO_3, PDF#00-033-0596) (Fig. 1(a)). This is primarily due to the tendency of B_4C particle surfaces to adsorb oxygen, leading to the formation of B_2O_3. Owing to its high hygroscopic nature, B_2O_3 readily reacts with atmospheric moisture to form boric acid [34]. The B_4C powder exhibited a uniform polyhedral morphology with an average particle size of 0.97 μm (Fig. 1(b)).

For the as-synthesized $Y_3Si_2C_2$ powder, the dominant diffraction peaks can be

indexed to the $Y_3Si_2C_2$ phase (PDF#00-051-0835), accompanied by minor peaks corresponding to Y_2O_3 (PDF#04-010-3289) (Fig. 1(a)). The presence of a small amount of Y_2O_3 is mainly attributed to the high chemical reactivity of YH_2, which readily adsorbs oxygen. Complete exclusion of air and moisture during processing is challenging, leading to partial oxidation of YH_2 to yttrium oxide. This observation is consistent with previously reported results [35, 36]. The $Y_3Si_2C_2$ powder showed a layered morphology with a mean particle size of 1.96 μm (Fig. 1(c)).

The XRD patterns of the mixed powders can be fully indexed to B_4C, $Y_3Si_2C_2$ and Y_2O_3, with no additional phases detected (Fig. 1(a)). This indicates that no significant solid-state reactions occurred during powder processing. As shown in Fig. 1(d), the constituent powders were homogeneously distributed, confirming effective mixing.

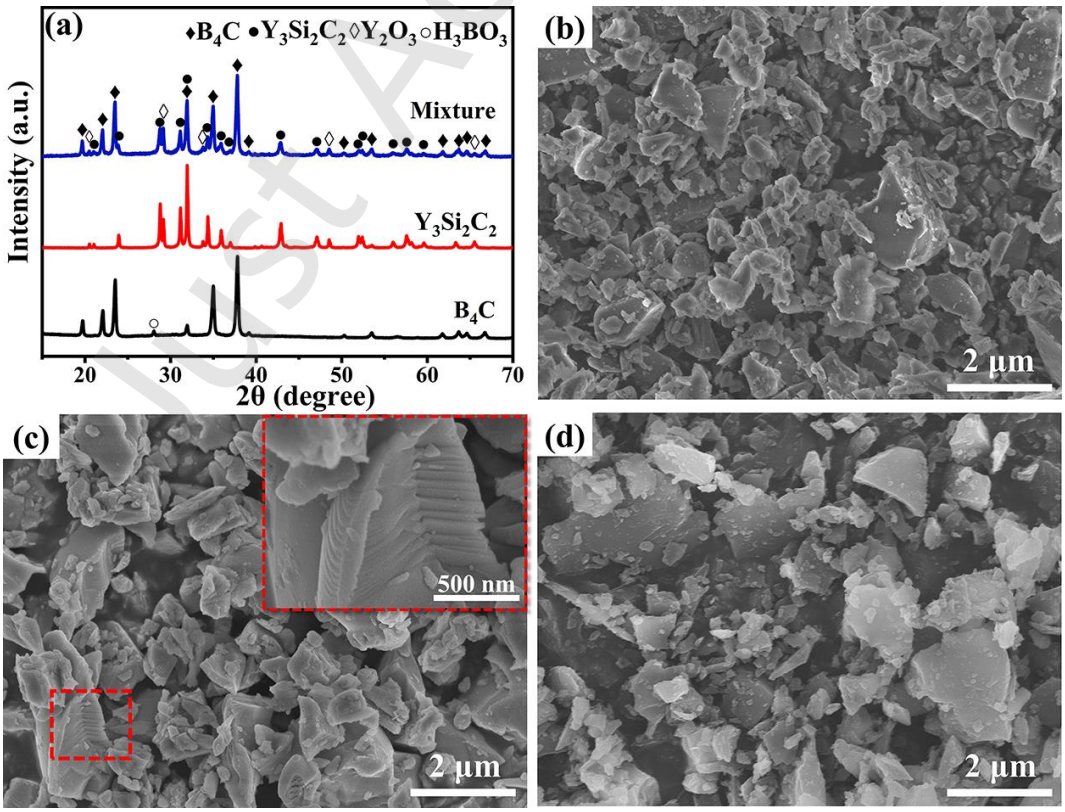

Fig.1 (a) XRD patterns of the B_4C, $Y_3Si_2C_2$ and mixed 8 wt.% $Y_3Si_2C_2/B_4C$ powders;

SEM image of (b) B_4C powder, (c) $Y_3Si_2C_2$ powder, (d) 8 wt.% $Y_3Si_2C_2/B_4C$ mixture.

3.2 Apparent density and relative density of the as-obtained B_4C ceramics

Fig. 2 illustrates the apparent and relative densities of B_4C ceramics with various contents of $Y_3Si_2C_2$ additive sintered at 1700 °C, as well as the specimens containing 8 wt.% $Y_3Si_2C_2$ (8 wt.% $Y_3Si_2C_2/B_4C$) sintered at temperatures between 1700 °C and 1900 °C. At the sintering temperature of 1700 °C, the relative density of the B_4C ceramics significantly increased from 82.14% to 95.56% as the $Y_3Si_2C_2$ content increased from 0 wt.% to 10 wt.%. This indicates that the addition of $Y_3Si_2C_2$ remarkably promoted the densification of B_4C ceramics. However, a further increase in the $Y_3Si_2C_2$ additive content to 12 wt.% resulted in a reduction in relative density to 89.1%, accompanied by the increased porosity within the ceramic matrix. Notably, the relative densities of the samples containing 8 wt.% and 10 wt.% were comparable (95.52% and 95.56%, respectively), suggesting that 10 wt.% represents the optimal or saturation level for $Y_3Si_2C_2$ addition. Accordingly, compositions with $Y_3Si_2C_2$ contents in the range of 0 - 10 wt.% were selected for subsequent investigation.

In addition, the relative density of the 8 wt.% $Y_3Si_2C_2/B_4C$ initially increased and subsequently decreased as the sintering temperature increased from 1700 °C to 1900 °C, reaching a maximum value of 98.13% at 1800 °C before declining to 97.39% at 1900 °C. This behavior may be attributed to an increase in residual porosity resulting from the evaporation of the liquid phase formed at elevated temperatures.

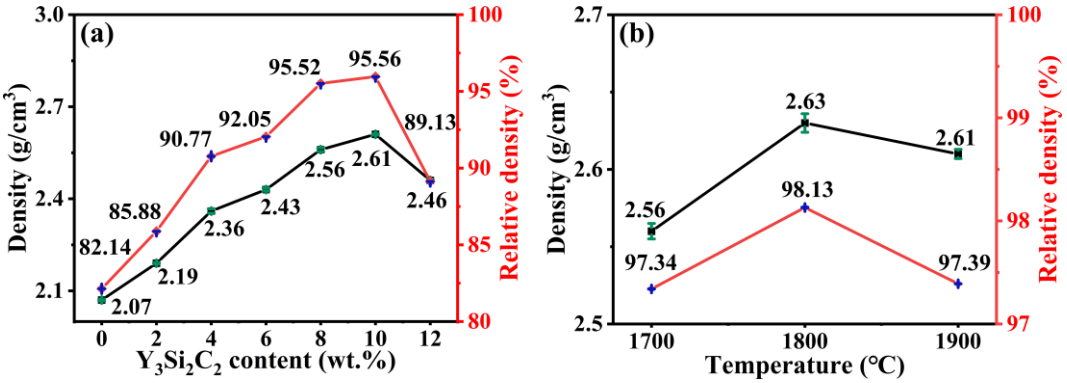

Fig. 2 Apparent and relative densities of B_4C ceramics: (a) containing various amounts of $Y_3Si_2C_2$ additive, (b) containing 8 wt.% $Y_3Si_2C_2$ additive and sintered at different temperatures.

3.3 Microstructure and phase compositions of the as-obtained B_4C ceramics

Fig. 3 and Fig. 4 present the phase compositions and microstructural characteristics of B_4C ceramics containing different contents of $Y_3Si_2C_2$ sintered at 1700 °C, as well as the 8 wt.% $Y_3Si_2C_2$/B_4C ceramics sintered at temperatures between 1700 °C and 1900 °C, respectively. At the sintering temperature of 1700 °C, only diffraction peaks corresponding to B_4C were detected for the monolithic B_4C ceramics, with no evidence of H_3BO_3 impurity phase (Fig. 3(a)). This confirms that the H_3BO_3 present in the raw B_4C powder was completely dehydrated and volatilized during high-temperature sintering.

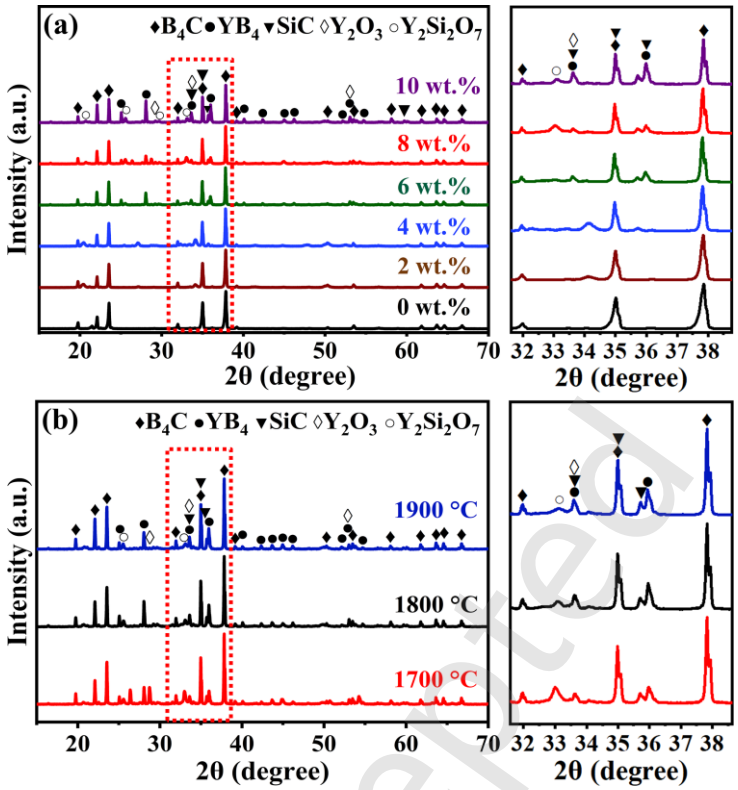

Fig. 3 XRD patterns of B_4C ceramics: (a) with varying $Y_3Si_2C_2$ additive content, (b) with 8 wt.% $Y_3Si_2C_2$ additive and sintered at different temperatures.

With the incorporation of the $Y_3Si_2C_2$ sintering additive, additional diffraction peaks corresponding to YB_4, SiC, Y_2O_3, and $Y_2Si_2O_7$ were detected (Fig. 3(a)), with their intensities increasing progressively with increasing $Y_3Si_2C_2$ content. Notably, no diffraction peaks associated with $Y_3Si_2C_2$ were detected, indicating that $Y_3Si_2C_2$ undergoes chemical transformation during the sintering process (Fig. 3(a)).

As the sintering temperature was increased from 1700 °C to 1900 °C, these Y-containing phases, along with SiC, remained present without the formation of additional phases (Fig. 3(b)). This suggests that phase evolution was primarily governed by reactions involving $Y_3Si_2C_2$, and that increasing the sintering temperature did not alter the fundamental reaction pathways.

As shown in Fig. 4(a-f)), the apparent pores in the B_4C ceramics decreased significantly with increasing $Y_3Si_2C_2$ content. This trend is consistent with the corresponding increase in relative density, indicating that $Y_3Si_2C_2$ effectively promotes the densification of B_4C ceramics. The enhanced densification can be primarily attributed to the formation of Y-rich liquid phase, together with solid YB_4 and other reaction-derived phases generated via multistage reactions of $Y_3Si_2C_2$ during the sintering process. The Y-rich liquid phase not only facilitates particle rearrangement and enhances diffusion kinetics, but also synergistically fills intergranular voids. This significantly increases the relative density of the B_4C ceramics and enables densification at reduced sintering temperatures.

Furthermore, the introduction of the secondary phase constituents effectively suppresses grain growth, reducing the average grain size from 1.10 μm for monolithic B_4C (0 wt.%) to 0.99 μm for the sample containing 10 wt.% $Y_3Si_2C_2$ (Fig. 4(i-n)).When the sintering temperature was increased from 1700 °C to 1900 °C, a small amount of residual porosity was still observed in the 8 wt.% $Y_3Si_2C_2/B_4C$ ceramics (Fig. 4(e) and 4(g-h)), which can be attributed to the volatilization of Y-rich liquid phase at elevated temperatures. At the same time, higher sintering temperatures promoted grain coarsening. The average grain sizes of the samples sintered at 1700 °C, 1800 °C, and 1900°C were 0.99 ± 0.02 μm, 1.20 ± 0.04 μm, and 1.50 ± 0.02 μm, respectively (Fig. 4(m) and 4(o-p)).

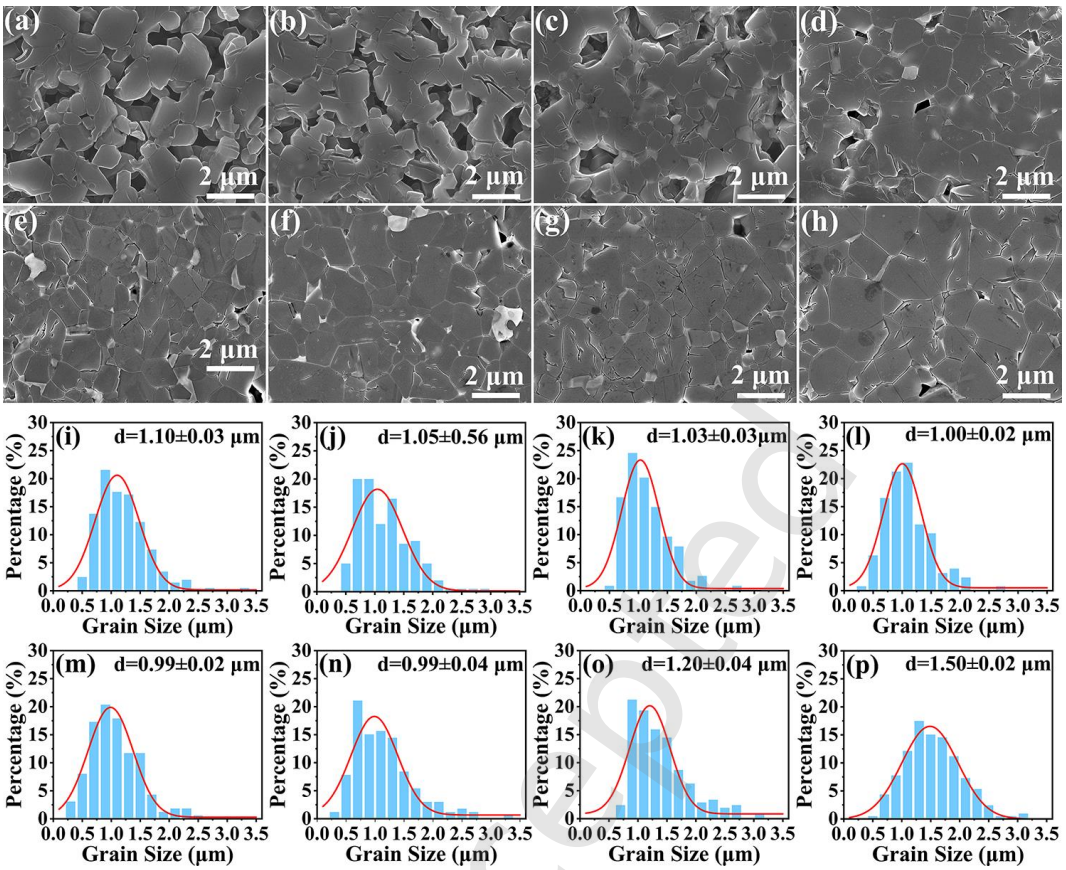

Fig. 4 SEM images of the microstructures and the grain size distribution of B_4C ceramics: (a) and (i) 17-0, (b) and (j) 17-2, (c) and (k) 17-4, (d) and (l) 17-6, (e) and (m) 17-8, (f) and (n) 17-10, (g) and (o) 18-8, (h) and (p) 19-8.

The phase composition and interfacial characteristics of the 8 wt.% $Y_3Si_2C_2/B_4C$ ceramics sintered at 1800 °C (sample 18-8) were further investigated by TEM, SAED and EDS. The corresponding results are shown in Fig. (5)-(9) and summarized in Table 1. Based on combined EDS and SAED analysis, multiple phases were identified within the representative region shown in Fig. 5(a). Point 1 was identified as SiC, for which an interplanar spacing of d = 0.253 nm measured along the $[\bar{2}02]$ direction corresponds to the SiC (111) plane (PDF#04-010-5699, Fig. 6(b)). Point 2 exhibits a lattice-fringe spacing of d = 0.257 nm along the [812] direction, consistent with the B_4C

($\bar{1}04$) plane (PDF#00-035-0798, Fig. 6(c)), confirming that this region corresponds to the B_4C matrix. Points 3 and 4 were identified as Y-containing phases. Specifically, point 3 shows an interplanar spacing of d = 0.395 nm along the [$1\bar{1}0$] direction, corresponding to the YB_4 (001) plane (PDF#04-004-8617, Fig. 7(b)), while point 4 exhibits a spacing of d = 0.841 nm along the [020] direction, consistent with the Y_2O_3 ($00\bar{1}$) plane (PDF#04-001-8726, Fig. 8(b)). The SAED results are consistent with the XRD analysis.

The $Y_2Si_2O_7$ phase was not detected in the region shown in Fig. 5(a), possibly due to its low volume fraction and the limited sampling area of the FIB-prepared specimen. The secondary-phase particles were tightly bonded to the B_4C matrix, with no obvious interfacial defects, elemental segregation, or residual porosity, indicating the formation of stable and well-integrated phase interfaces.

In addition, HAADF-EDS elemental mapping (Fig. 9(a-f)) reveals a narrow, band-like Y-enriched region, an approximate width of 4.3 nm, located between adjacent B_4C grains. The B, C, Si, and O elements were uniformly distributed within the matrix, whereas Y exhibited pronounced local enrichment, indicating distinct Y segregation at specific regions. When combined with the XRD results, these observations indicate that $Y_3Si_2C_2$ reacts at elevated temperatures, leading to the formation of a Y-rich liquid phase. Under uniaxial compressive stress during sintering, the Y-rich liquid phase preferentially diffuses along grain boundaries, forming rapid diffusion pathways that promote atomic rearrangement and mass transport within the B_4C matrix. This process

accelerates grain boundary migration and effectively reduces the required sintering temperature.

The rapid cooling process promotes the precipitation and solidification of residual Y-rich liquid phases at grain boundaries, forming Y-enriched interfacial zones. Previous studies have reported similar Y segregation behavior at B_4C grain boundaries [37]. Such segregation modifies the local chemical composition of the grain boundaries and reduces interfacial bonding strength. The weakened interface strength promotes the occurrence of intergranular fracture mechanisms during crack propagation.

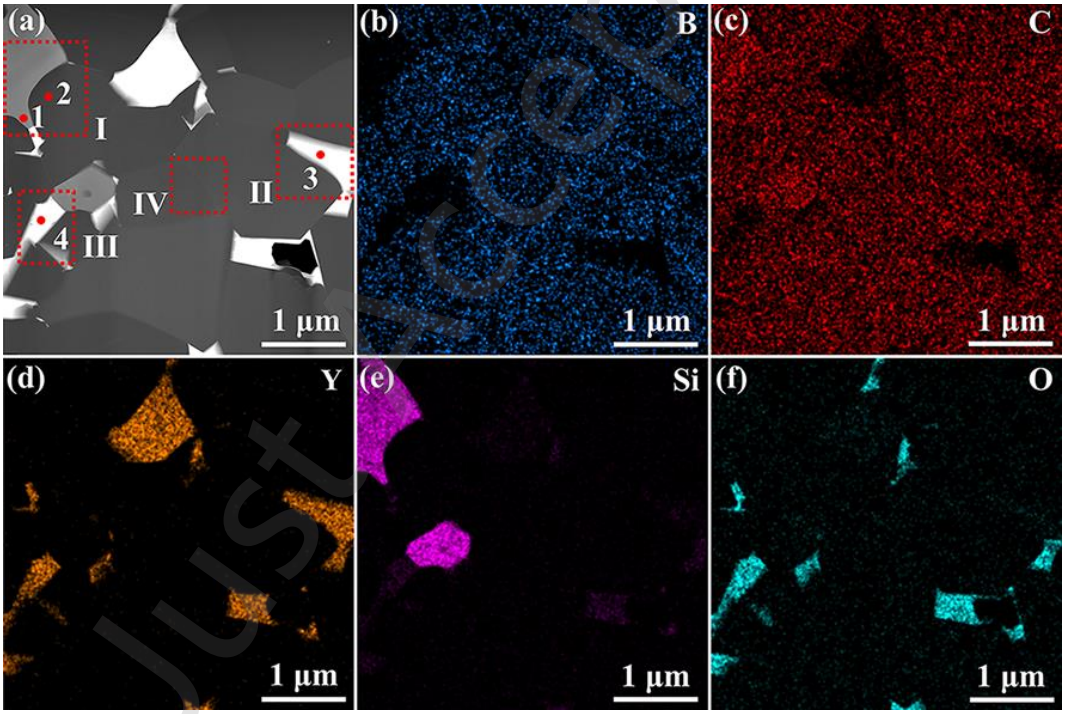

Fig. 5 (a) HAADF image of the 18-8 sample; elemental distribution maps showing (b) B-rich region, (c) C-rich region, (d) Y-rich region, (e) Si-rich region, and (f) O-rich region.

Table1 EDS elemental compositions obtained from points 1-4 in Fig. 5(a)

NO.	Composition in atomic %					Probable phase
	B	C	Y	Si	O	

1	0.00	27.01	0.20	69.94	2.84	Si-C
2	50.22	43.33	0.19	1.48	4.78	B-C
3	4.80	0.20	91.01	0.00	3.99	Y-B
4	0.00	3.16	40.40	4.74	51.70	Y-O, Y-Si-O

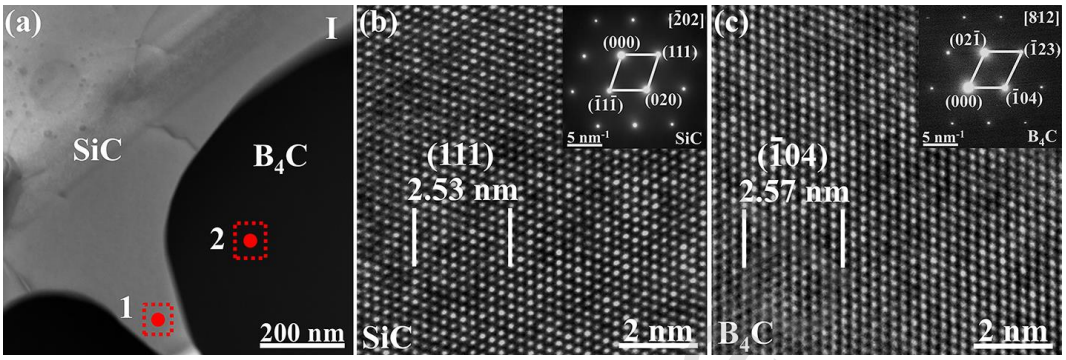

Fig. 6 (a) Enlarged view of region I as indicated in Fig. 4(a), (b) HRTEM image corresponding to Point 1 (SiC), (c) HRTEM image of Point 2 (B_4C).

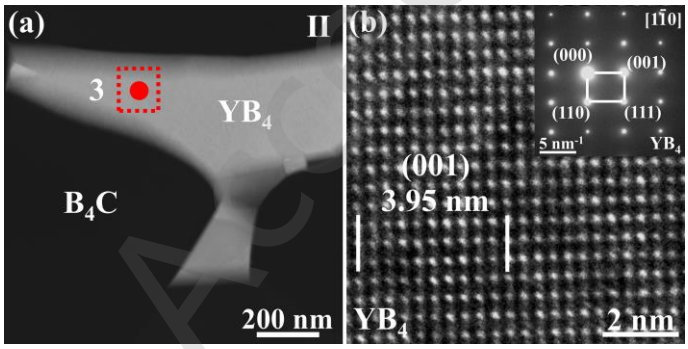

Fig. 7 (a) Enlarged view of region II as indicated in Fig. 4(a), (b) HRTEM image corresponding to Point 3 (YB_4).

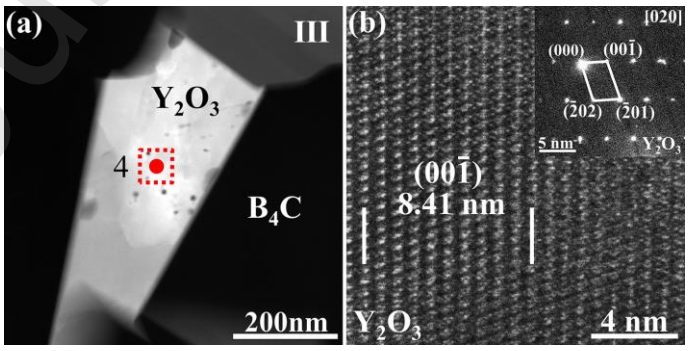

Fig. 8 (a) Enlarged view of region III as indicated in Fig. 4(a), (b) HRTEM image corresponding to Point 4 (Y_2O_3).

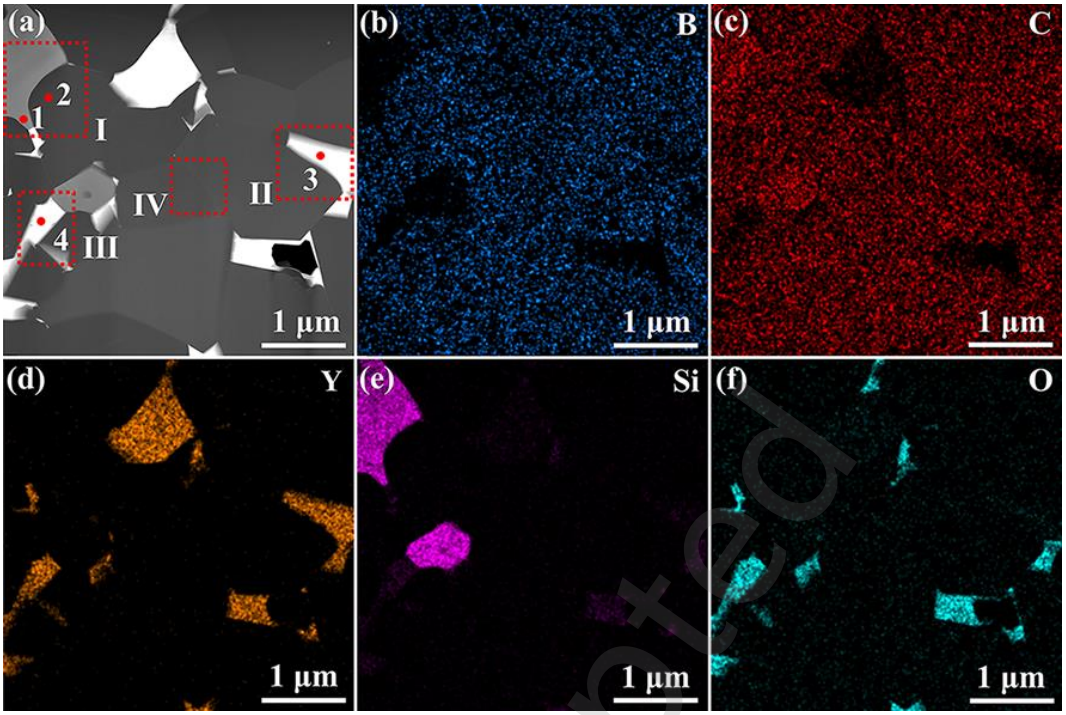

Fig.9 (a) Enlarged view of region IV as indicated in Fig. 4(a), (b) B-rich region, (c) C-rich region, (d) Y-rich region, (e) Si-rich region, (f) O-rich region.

3.4 Thermal conductivity and electrical conductivity

Room temperature thermal conductivity and electrical conductivity of B_4C ceramics with varying $Y_3Si_2C_2$ sintering-additive contents (sintered at 1700 °C) and at different sintering temperatures for 8 wt.% $Y_3Si_2C_2/B_4C$ are summarized in Table 2. The thermal conductivity of the B_4C ceramics increased with the increasing $Y_3Si_2C_2$ content, with the 17-10 sample exhibiting the highest value of 21.9 $W \cdot m^{-1} \cdot K^{-1}$, representing a 56.75% improvement over that of monolithic B_4C (14.0 $W \cdot m^{-1} \cdot K^{-1}$). This enhancement is mainly attributed to the improved densification caused by the $Y_3Si_2C_2$ sintering additive, which forms a liquid phase during sintering and fills intergranular pores, thereby reducing phonon scattering associated with porosity [38]. Additionally, the decomposition of $Y_3Si_2C_2$ generates cubic β-SiC phase, which possesses a high

theoretical thermal conductivity of up to 490 $W \cdot m^{-1} \cdot K^{-1}$ [39], further contributing to the overall thermal conductivity. The interfaces between the secondary phase particles and the B_4C matrix are clean, with no obvious impurity segregation or residual porosity, minimizing interfacial phonon scattering. Furthermore, as the sintering temperature of 8 wt.% $Y_3Si_2C_2/B_4C$ ceramics increased from 1700 °C to 1900 °C, the average grain size increased from 0.99 μm to 1.50 μm. This grain coarsening further reduces phonon scattering at grain boundaries, promoting a continuous increase in thermal conductivity from 19.4 $W \cdot m^{-1} \cdot K^{-1}$ (1700 °C) to 20.4 $W \cdot m^{-1} \cdot K^{-1}$ (1900 °C).

The electrical conductivity of monolithic B_4C ceramics was 1.7 $S \cdot cm^{-1}$. As the $Y_3Si_2C_2$ content increases, the conductivity of the ceramics gradually increases; reaching 3.0 $S \cdot cm^{-1}$ at a 10 wt.% $Y_3Si_2C_2$ addition. This enhancement is primarily attributed to increased relative density, grain boundary refinement, and the formation of the highly conductive YB_4 phase (3.3×10^4 $S \cdot cm^{-1}$ [40]). Furthermore, as the sintering temperature increased from 1700 °C to 1900 °C, the electrical conductivity of the 8 wt.% $Y_3Si_2C_2/B_4C$ ceramics increased from 2.9 $S \cdot cm^{-1}$ to 3.4 $S \cdot cm^{-1}$. While grain growth at higher temperatures reduces electron scattering and lowers electrical resistance, the overall improvement in electrical conductivity remained moderate due to the limited extent of microstructural changes.

Table 2 Apparent density, relative density, and physical properties of B_4C samples sintered with varying $Y_3Si_2C_2$ content and the 8 wt.% $Y_3Si_2C_2/B_4C$ sintered at different temperatures.

Sample (°C/wt.%)	Density ($g \cdot cm^{-3}$)	Relative Density (%)	Thermal conductivity ($W \cdot m^{-1} \cdot K^{-1}$)	Electrical conductivity ($S \cdot cm^{-1}$)
17-0	2.07	82.14	14.0±0.01	1.7±0.14
17-2	2.19	85.55	16.1±0.04	2.2±0.05
17-4	2.36	90.77	17.8±0.05	2.6±0.11
17-6	2.43	92.05	17.1±0.02	2.9±0.05
17-8	2.56	95.52	19.4±0.06	2.9±0.03
17-10	2.61	95.96	21.9±0.12	3.0±0.06
18-8	2.63	98.13	20.3±0.16	3.0±0.07
19-8	2.61	97.39	20.4±0.16	3.4±0.03

3.5 Mechanical properties

Fig. 10 shows the Vickers hardness of B_4C ceramics sintered with varying $Y_3Si_2C_2$ contents at 1700 °C, and at different sintering temperatures for the samples containing 8 wt.% $Y_3Si_2C_2$. The results indicated that, for the specimens sintered at 1700 °C, the Vickers hardness initially increased and then decreased with increasing $Y_3Si_2C_2$ content. The 17-8 sample exhibited the highest hardness value of 30.7 GPa, which is approximately three times greater than that of monolithic B_4C ceramics (11.3 GPa). This significant improvement is attributed to the enhanced relative density, refined grain size, and improved grain boundary purity. However, with a further increase in $Y_3Si_2C_2$ content to 10 wt.%, the hardness slightly decreased to 30.3 GPa, which is associated with the formation of a higher fraction of secondary phases with relatively low hardness [41]. Moreover, the Vickers hardness of 8 wt.% $Y_3Si_2C_2/B_4C$ ceramics sintered at 1700 °C, 1800 °C, and 1900 °C was 30.7 GPa, 31.4 GPa, and 29.9 GPa, respectively. The reduction in hardness observed at 1900 °C is mainly attributed to excessive grain growth, which adversely affects the mechanical properties [42].

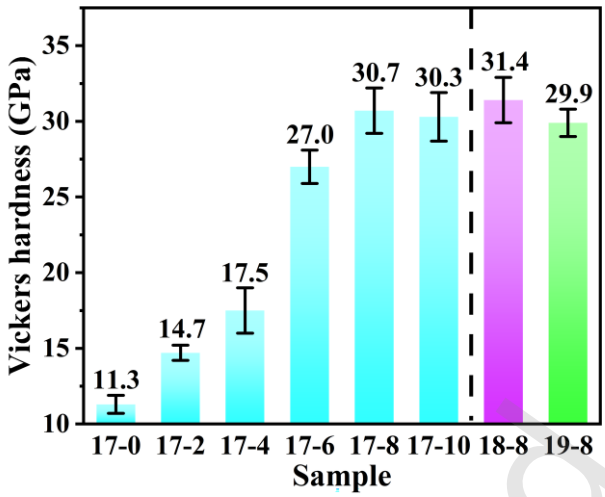

Fig.10. Vickers Hardness of B_4C ceramics with varying amounts of $Y_3Si_2C_2$ additive, and B_4C with 8 wt.% $Y_3Si_2C_2$ sintered at different temperatures

Fig. 11 shows the flexural strength of B_4C ceramics with varying $Y_3Si_2C_2$ contents sintered at 1700 °C, as well as those samples containing 8 wt.% $Y_3Si_2C_2$ sintered at different temperatures. As the $Y_3Si_2C_2$ content increased from 0 wt.% to 8 wt.%, the flexural strength of the B_4C ceramics increased markedly from 362.5 MPa to 585.5 MPa, corresponding to an improvement of 61.52%. This enhancement is primarily attributed to the progressive reduction in porosity and the accompanying grain refinement achieved during sintering at 1700 °C with increasing additions of $Y_3Si_2C_2$ (Fig. (4)-(5)). According to the Hall-Petch relationship [43], both the increased relative density and the grain refinement contribute to the observed improvement of the flexural properties. However, when the content of the secondary phases with relatively low mechanical strength exceeds a critical level, the overall mechanical performance begins to deteriorate. Consequently, upon increasing the $Y_3Si_2C_2$ content to 10 wt.%, the flexural strength of the B_4C ceramic slightly decreased to 568.5 MPa.

It was further investigated that the flexural strength of 8 wt.% $Y_3Si_2C_2$/B_4C initially increased and subsequently decreased with increasing sintering temperatures, reaching the values of 585.5 MPa, 694.0 MP and 427.0 MPa at 1700 °C, 1800 °C and 1900 °C, respectively. Due to the difficulty in achieving full densification of B_4C, obtaining high flexural strength at lower sintering temperatures is challenging. However, the maximum flexural strength of 694.0 MPa observed for the sample sintered at 1800 °C is comparable to several high-performance B_4C -based composites reported in the literature (Fig. 13), particularly considering its relatively low sintering temperature. The enhancement in strength with increasing temperature is primarily attributed to improved densification, while the subsequent reduction in strength is mainly caused by the detrimental effect of grain coarsening. As the sintering temperature increased, the grain size of 8 wt.% $Y_3Si_2C_2$/B_4C ceramics gradually increased, with particularly severe grain growth occurring at 1900 °C, which led to a pronounced reduction in flexural strength at this temperature [44].

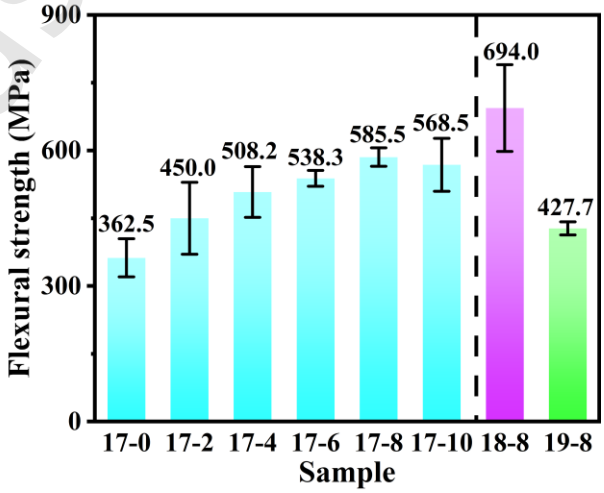

Fig.11 Flexural strength of B_4C ceramics with varying amounts of $Y_3Si_2C_2$ additive

and B_4C ceramics with 8 wt.% $Y_3Si_2C_2$ sintered at different temperatures.

Fig. 12 shows the fracture surface morphology of the investigated ceramics. The fracture surface of monolithic B_4C was relatively smooth, whereas the incorporation of $Y_3Si_2C_2$ as a sintering additive preserved the overall smoothness with locally roughened features. As a result, the fracture mechanism shifts from predominantly transgranular fracture in monolithic B_4C ceramics to a mixed transgranular-intergranular fracture mode in X wt.% $Y_3Si_2C_2/B_4C$ ceramics. The transgranular fracture enhances energy dissipation during crack propagation, thereby improving the flexural strength, while the intergranular fracture is beneficial for enhancing fracture toughness [45].

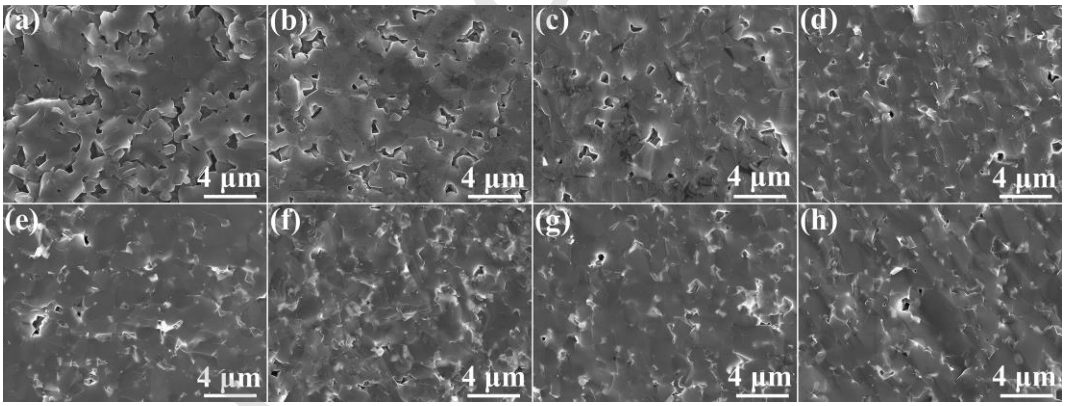

Fig. 12 SEM images of the fracture surfaces of B_4C ceramics with different $Y_3Si_2C_2$ contents and B_4C ceramics with 8 wt.% $Y_3Si_2C_2$ sintered at different temperatures: (a) 17-0, (b) 17-2, (c) 17-4, (d) 17-6, (e) 17-8, (f) 17-10, (g) 18-8, (h) 19-8.

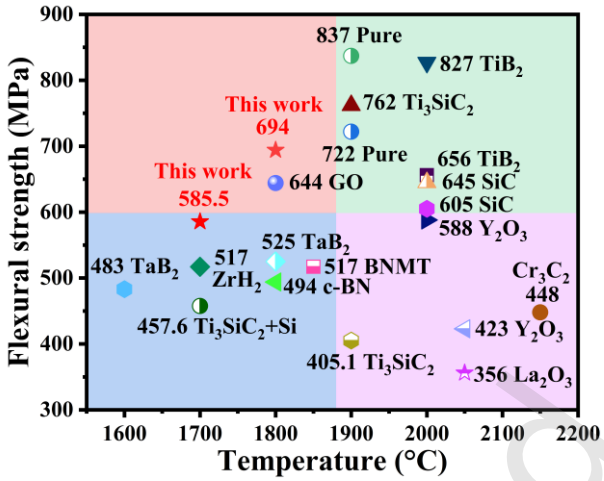

Fig. 13 The flexural strength of B_4C ceramics sintered with 8 wt.% $Y_3Si_2C_2$ additive at different temperatures (the work presented herein), and their comparison with earlier studies on B_4C ceramics sintered with various additives[46-53].

3.6 Discussion of sintering mechanism

In order to reveal the sintering mechanism and the interface reaction among B_4C, $Y_3Si_2C_2$, and the possible oxides of Y_2O_3, SiO_2, and B_2O_3 in the system, the 10 wt. % $Y_3Si_2C_2/B_4C$ was additionally sintered at temperatures ranging from 800 °C to 1600 °C. Fig. 14 illustrates the X-ray diffraction (XRD) patterns and the corresponding phase evolution of the samples sintered at different temperatures. At 800 °C, the characteristic diffraction peaks of B_4C and $Y_3Si_2C_2$ were predominantly observed, indicating that the $Y_3Si_2C_2$ additive remains crystallographically stable and does not undergo reaction at this temperature.

Upon increasing the sintering temperature to 1000 °C, the diffraction peaks associated with $Y_3Si_2C_2$ vanished completely, accompanied by the emergence of peaks corresponding to Y_2SiO_5 (yttrium silicate). Given that the melting and decomposition

temperature of $Y_3Si_2C_2$ (~ 1590 °C [32]) is significantly higher than the applied temperature, this transformation is attributed to oxidative decomposition rather than thermal decomposition. Due to its strong oxygen affinity [30], $Y_3Si_2C_2$ is inferred to scavenge oxygen from B_2O_3 and H_2O(generated via H_3BO_3 decomposition (Equation (1) [54]), leading to the formation of Y_2SiO_5 (Equation (2)) [31]. In addition, Y_2SiO_5 phase was also detected when the $Y_3Si_2C_2$ coating oxidation in both ambient air and wetoxygen [31]. On the other hand, the strong oxygen-gettering ability of $Y_3Si_2C_2$ could purify the oxide film on the surface of boron carbide, thereby promoting its sintering, which observed in Si_3N_4 ceramics sintered with $RE_3Si_2C_2$ additives [30, 55, 56].

Given that B_4C exhibits strong reducing properties at high temperatures, it reacts with oxygen-containing substances to undergo reduction reactions. As the sintering temperature is further increased to 1200 °C, a new diffraction peak corresponding to the YB_4 phase was detected, while Y_2SiO_5 remained present. This indicates that elevated temperatures facilitate solid-state reactions between yttrium-containing species (e.g., Y_2SiO_5) and the B_4C matrix, leading to the formation of YB_4 (Equation (3)). However, the persistence of Y_2SiO_5 suggests that the reaction is not yet complete. The formation of the thermodynamically stable YB_4 phase, which preferentially nucleates at grain boundaries, can contribute to the inhibition of grain growth.

At higher temperatures of 1400-1600 °C, diffraction peaks of $Y_5BSi_2O_{13}$ (yttrium borosilicate) were detected, whereas the Y_2SiO_5 peaks disappeared. This suggests that at these temperatures, Y_2SiO_5 reacts with oxide species, such as B_2O_3 and Y_2O_3, to form

$Y_5BSi_2O_{13}$(Equation (4))[57]. Considering that $Y_5BSi_2O_{13}$ undergoes vitrification between 300 °C and 1200 °C and exhibits melting behavior at ~ 1000 °C [58], it can be inferred that $Y_5BSi_2O_{13}$ forms a Y-B-Si-O quaternary liquid phase at elevated temperatures. The presence of this liquid phase enhances mass transport, facilitating particle rearrangement and diffusion, thereby promoting densification.

Due to the rapid crystallization kinetics of $Y_5BSi_2O_{13}$ from the glassy state [58], the majority of this phase exists in crystalline form and is therefore detectable by XRD, while a minor fraction remains as an amorphous phase within the microstructure. The Yttrium-rich regions observed in Fig. 9 provide further evidence of liquid-phase sintering and the retention of residual liquid phases. As the sintering temperature continues to increase, the Y-B-Si-O liquid phase further reacts with the B_4C matrix. During this process, silicon-containing species are reduced by carbon to form SiC, while thermodynamically stable phases, such as YB_4, Y_2O_3, and SiC, are simultaneously generated. These reaction products contribute to pore filling and enhanced densification. On the other hand, a eutectic liquid phase could be formed in the Y_2O_3-SiO_2 system at high temperature of ~ 1700 °C [59], which could enhanced mass transport and improved the consolidation of the B_4C.

In summary, the sintering mechanism of B_4C ceramics with $Y_3Si_2C_2$ as a sintering additive can be described by two primary pathways: (i) an in-situ reaction mechanism involving the Y_2SiO_5 intermediate within the Y-Si-B-O quaternary system, and (ii) liquid-phase sintering associated with the formation of a Y-Si-B-O quaternary liquid-

phase and Y-Si-O liquid phase, as illustrated in Fig. 15.

$$2H_3BO_3=B_2O_3+3H_2O \quad (1)$$

$$2Y_3Si_2C_2+\frac{21}{2}O_2=3Y_2SiO_5+SiO_2+4CO \quad (2)$$

$$Y_2SiO_5+2B_4C=2YB_4+SiO_2+CO+CO_2 \quad (3)$$

$$2Y_2SiO_5+\frac{1}{2}Y_2O_3+\frac{1}{2}B_2O_3=Y_5BSi_2O_{13} \quad (4)$$

$$Y_2SiO_5+SiO_2=Y_2Si_2O_7 \quad (5)$$

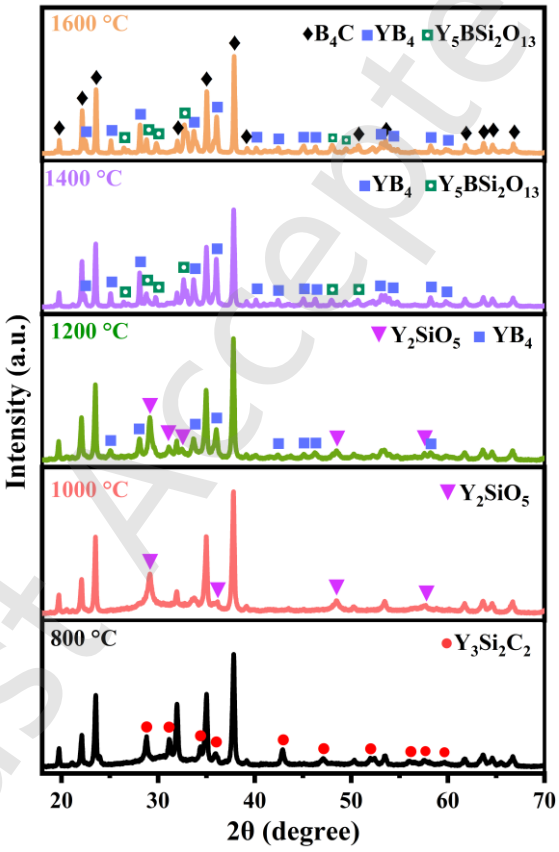

Fig. 14 XRD patterns of 10 wt.% $Y_3Si_2C_2$/B_4C at different temperatures.

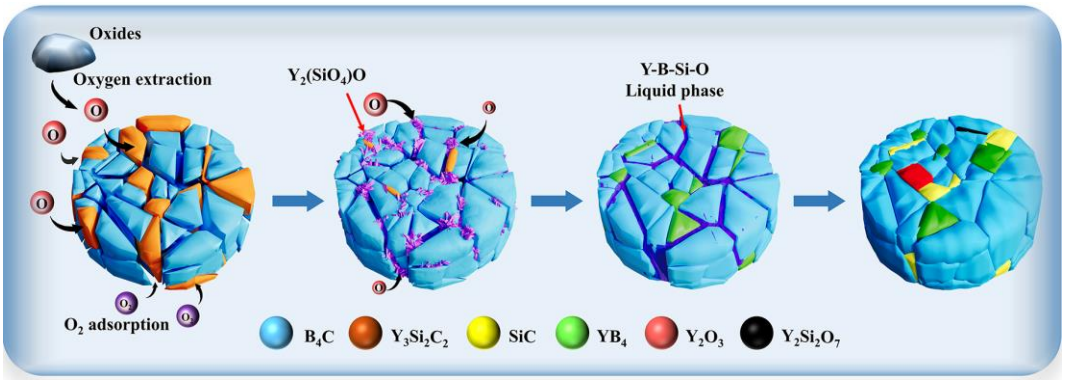

Fig. 15 Reaction mechanism involved in the sintering of B_4C ceramics using $Y_3Si_2C_2$ as a sintering additive.

Conclusion

In this study, dense B_4C ceramics were successfully fabricated by spark plasma sintering (SPS) using novel sintering additive of $Y_3Si_2C_2$. At a sintering temperature of 1700 °C, a systematic investigation of $Y_3Si_2C_2$ content revealed that an addition of 8 wt.% resulted in the highest hardness and flexural strength, reaching 30.7 GPa and 585.5 MPa, respectively. Therefore, this was identified as the optimal additive concentration. Subsequently, B_4C ceramics containing 8 wt.% $Y_3Si_2C_2$ were further sintered in the temperature range of 1700-1900 °C. The optimum overall mechanical performance was achieved at 1800 °C, where the hardness, and flexural strength reached 31.4 GPa, and 694 MPa, respectively. These improvements are primarily attributed to the strong oxygen affinity of $Y_3Si_2C_2$ and the multistage reaction mechanisms it induces. Initially, $Y_3Si_2C_2$ adsorbs oxygen to form an in-situ Y_2SiO_5 intermediate phase. This intermediate phase reacts with the B_4C matrix to generate the YB_4 strengthening phase and simultaneously interacts with oxides to form a Y-Si-B-O quaternary liquid phase. In addition, a eutectic liquid phase could be formed in the

Y_2O_3-SiO_2 system at high temperature. Under applied sintering pressure, the yttrium-rich liquid phase infiltrates grain boundaries, effectively promoting particle rearrangement and mass transport. Furthermore, the in situ-generated YB_4 phase contributes to densification while inhibitting excessive grain growth. Overall, $Y_3Si_2C_2$ is demonstrated to be an effective sintering additive, which significantly enhances both the densification and mechanical properties of B_4C ceramics.

Acknowledgements

This study was supported by the National Natural Science Foundation of China (Grant No.12275337, U2330103, and 11975296), Zhejiang Provincial Natural Science Foundation of China under Grant No.LZ24A050004. We would like to recognize the support from the Ningbo Youth Science and Technology Innovation Leading Talent Project (2023QL043) and International Exchange Projects of the 9th Meeting of the China Slovakia Science and Technology Cooperation Committee (No.9-6).

Availability of data and materials

The data that support the findings of this study are available from the corresponding author upon reasonable request.

Competing interests

The authors have no competing interests to declare that are relevant to the content of this article.

Author contributions

Lirui He: Writing-original draft, Methodology, Investigation, Formal analysis, Data curation. Pengxing Cui: Software, Formal analysis. Gang Qin: Methodology, Formal analysis. Bin Wang: Software, Formal analysis. Tiantian Tao: Formal analysis. Xiaobing Zhou: Writing review & editing, Supervision, Resources, Project

administration, Funding acquisition, Conceptualization.

References

[1] Zhao ZQ, Liao W, Chen J, *et al.* Advanced research on the preparation and application of carbide ceramic fibers. *J Adv Ceram*. 2024, **13(9)**: 1291-1336.

[2] Li XG, Jiang DL, Zhang JX, *et al.* Densification behavior and related phenomena of spark plasma sintered boron carbide. *Ceram Int*. 2014, **40(3)**: 4359-4366.

[3] Turatti AM, Pereira AS. Wear resistant boron carbide compacts produced by pressureless sintering. *Ceram Int*. 2017, **43(11)**: 7970-7977.

[4] Zhao K, Zhong WM, Sun MY, *et al.* Sintering Mechanism of Pure B_4C Ceramic Prepared by Hot Oscillating Pressing and with Excellent Mechanical Properties. *Adv Eng Mater*. 2024, **26(16)**: 2400695.

[5] Wang H, Zeng Y, Dai YJ, *et al.* Enhanced mechanical properties of boron carbide ceramics prepared by spark plasma sintering with boron nitride nanosheets addition. *J Eur Ceram. Soc*. 2024, **44(15)**: 116735.

[6] Qu ZX, Yu CJ, Wei YT, *et al.* Thermal conductivity of boron carbide under fast neutron irradiation. *J Adv Ceram*. 2022, **11(3)**: 482-494.

[7] Pramanick A, Dey PP, Das PK. Microstructure, phase and electrical conductivity analyses of spark plasma sintered boron carbide machined with WEDM. *Ceram Int*. 2020, **46(3)**: 2887-2894.

[8] Liu GQ, Chen SX, Zhao YW, *et al.* The effect of transition metal carbides MeC (Me=Ti, Zr, Nb, Ta, and W) on mechanical properties of B_4C ceramics fabricated via

pressureless sintering. *Ceram Int*. 2020, **46(17)**: 27283-27291.

[9] Domnich V, Reynaud S, Haber RA*, et al.* Boron Carbide: Structure, Properties, and Stability under Stress. *J Am Ceram. Soc*. 2011, **94(11)**: 3605-3628.

[10] Suri AK, Subramanian C, Sonber JK*, et al.* Synthesis and consolidation of boron carbide: a review. *Int Mater. Rev*. 2010, **55(1)**: 4-40.

[11] Munir ZA, Quach DV, Ohyanagi M. Electric Current Activation of Sintering: A Review of the Pulsed Electric Current Sintering Process. *J Am Ceram Soc*. 2011, **94(1)**: 1-19.

[12] Liu YY, Ge S, Huang YH*, et al.* Influence of Sintering Process Conditions on Microstructural and Mechanical Properties of Boron Carbide Ceramics Synthesized by Spark Plasma Sintering. *Mat.* 2021, **14(5)**: 1100.

[13] Moshtaghioun BM, García DG, Rodríguez AD. High-temperature deformation of fully-dense fine-grained boron carbide ceramics: Experimental facts and modeling. *Mater Des*. 2015, **88**: 287-293.

[14] Moshtaghioun BM, Cumbrera-Hernández FL, Gómez-García D*, et al.* Effect of spark plasma sintering parameters on microstructure and room-temperature hardness and toughness of fine-grained boron carbide (B_4C). *J Eur Ceram Soc*. 2013, **33(2)**: 361-369.

[15] Grippi T, Torresani E, Maximenko AL*, et al.* Spark plasma sintering of boron carbide (B_4C): From characterisation to finite element modeling of sintering. *J Eur Ceram Soc*. 2024, **44(15)**: 116700.

[16] Moshtaghioun BM, Gomez-Garcia D, Dominguez-Rodriguez A, *et al.* Grain size dependence of hardness and fracture toughness in pure near fully-dense boron carbide ceramics. *J Eur Ceram Soc*. 2016, **36(7)**: 1829-1834.

[17] Sun C, Li YK, Wang YF, *et al.* Effect of alumina addition on the densification of boron carbide ceramics prepared by spark plasma sintering technique. *Ceram Int*. 2014, **40(8, Part B)**: 12723-12728.

[18] Vijay SK, Prabhu RK, Chandramouli V, *et al.* Sintering of nanocrystalline boron carbide synthesized by the B_2O_3-sucrose precursor method. *Ceram Int*. 2022, **48(16)**: 23878-23884.

[19] Sha WH, Liu YY, Zhou YB, *et al.* Effect of Carbon Content on Mechanical Properties of Boron Carbide Ceramics Composites Prepared by Reaction Sintering. *Mat.* 2022, **15(17)**: 6028.

[20] Ma LN, Xie KY, Toksoy MF, *et al.* The effect of Si on the microstructure and mechanical properties of spark plasma sintered boron carbide. *Mater Charact*. 2017, **134**: 274-278.

[21] Mashhadi M, Taheri-Nassaj E, Sglavo VM. Pressureless sintering of boron carbide. *Ceram Int*. 2010, **36(1)**: 151-159.

[22] Ebrahimi S, Heydari MS, Baharvandi HR, *et al.* Effect of iron on the wetting, sintering ability, and the physical and mechanical properties of boron carbide composites: A review. *Int J Refract Met Hard Mat.* 2016, **57**: 78-92.

[23] Roy TK, Subramanian C, Suri AK. Pressureless sintering of boron carbide. *Ceram*

Int. 2006, **32(3)**: 227-233.

[24] Yan QL, Zhou ZH, Yuan TC*, et al.* Effect of micro-doping yttrium oxide on hot-press sintering of boron carbide. *J Cent South Univ*. 2023, **30(9)**: 2919-2933.

[25] Yang M, Zhuang Y, Xing P. High-performance B_4C-LaB_6 composite ceramics fabricated via hot-pressing sintering with La_2O_3 as sintering additive. *Ceram Int.* 2021, **47(23)**: 32675-32684.

[26] Zamora V, Ojalvo C, Guiberteau F*, et al.* Fabricating ultrahard boron carbide–silicon carbide–zirconium diboride composites by spark plasma sintering from B_4C with $ZrSi_2$ aids. *J Eur Ceram Soc.* 2024, **44(6)**: 4323-4329.

[27] Qian ZJ, Xu H, Zhang XX*, et al.* Influence of silicon carbide addition on microstructural and compressive properties of boron carbide ceramics synthesized by reaction sintering. *Ceram Int*. 2025, **51(19, Part A)**: 27826-27834.

[28] Zhao J, Zhang XS, Ma ZN*, et al.* Tuning mechanical and electrical performances of B_4C–TiB_2 ceramics in a two-step spark plasma sintering process. *J Adv Ceram*. 2024, **13(4)**: 518-528.

[29] Ojalvo C, Guiberteau F, Ortiz AL. Fabricating toughened super-hard B_4C composites at lower temperature by transient liquid-phase assisted spark plasma sintering with $MoSi_2$ additives. *J Eur Ceram Soc*. 2019, **39(9)**: 2862-2873.

[30] Huang MZ, Huang Y, Ou J*, et al.* Effect of a new nonoxide additive, $Y_3Si_2C_2$, on the thermal conductivity and mechanical properties of Si_3N_4 ceramics. *Int J Appl Ceram. Technol*. 2022, **19(6)**: 3403-3409.

[31] Li Y, Chen ML, Zhang QZ, *et al.* Microstructure and corrosion behavior of in-situ grown $Y_3Si_2C_2$ coated SiC fibers exposed to air and wet-oxygen at 1400 °C. *J Eur Ceram Soc.* 2022, **42(8)**: 3427-3436.

[32] Zhou XB, Liu JW, Zou SR, *et al.* Almost seamless joining of SiC using an in-situ reaction transition phase of $Y_3Si_2C_2$. *J Eur Ceram Soc*. 2020, **40(2)**: 259-266.

[33] Shao JQ, Li M, Chang KK, *et al.* Fabrication and characterization of SPS sintered SiC-based ceramic from $Y_3Si_2C_2$-coated SiC powders. *J Eur Ceram Soc*. 2018, **38(15)**: 4833-4841.

[34] Wang S, Gao SB, Xing PF, *et al.* Pressureless liquid-phase sintering of B_4C with $MoSi_2$ as a sintering aid. *Ceram Int*. 2019, **45(10)**: 13502-13508.

[35] Shi LK, Zhou XB, Dai J-Q, *et al.* Microstructure and properties of nano-laminated $Y_3Si_2C_2$ ceramics fabricated via in situ reaction by spark plasma sintering. *J Adv Ceram*. 2021, **10(3)**: 578-586.

[36] Chen H, Zhao B, Zhao ZF, *et al.* Achieving strong microwave absorption capability and wide absorption bandwidth through a combination of high entropy rare earth silicide carbides/rare earth oxides. *J Mater Sci Technol.* 2020, **47**: 216-222.

[37] Baskut S, Ozer SC, Turan S. The effects of in-situ formed phases on the microstructure, mechanical properties and electrical conductivity of spark plasma sintered B_4C containing Y_2O_3. *J Eur Ceram Soc*. 2022, **42(4)**: 1272-1281.

[38] Wang XQ, Wu WT, Zhang Y, *et al.* Lightweight SiBCN-modified carbon-bonded carbon fiber composites with directional heat-leading function for efficient thermal

protection. *J Adv Ceram*. 2025, **14(7)**: 9221113.

[39] Zhang XY, Xie WQ, Sun L*, et al.* Continuous SiC skeleton reinforced highly oriented graphite flake composites with high strength and specific thermal conductivity. *J Adv Ceram*. 2022, **11(3)**: 403-413.

[40] Li J, Goto T, Hirai T 1998 Microstructure and thermoelectric properties of B-C-Y system composites. In: *Seventeenth International Conference on Thermoelectrics. Proceedings ICT98 (Cat. No.98TH8365),* pp 587-590

[41] Song WY, Lu YJ, Yang LT*, et al.* Enhancement of densification and mechanical property of $(Hf_{0.2}Zr_{0.2}Ti_{0.2}Nb_{0.2}Ta_{0.2})N$ high-entropy bulk ceramic via silicon carbide addition. *J Adv Ceram*. 2025, **14(1)**: 9221004.

[42] Zhang Y, Sun SK, Guo WM*, et al.* Optimal preparation of high-entropy boride-silicon carbide ceramics. *J Adv Ceram*. 2021, **10(1)**: 173-180.

[43] Cordero ZC, Knight BE, Schuh CA. Six decades of the Hall–Petch effect – a survey of grain-size strengthening studies on pure metals. *Inte Mater Rev*. 2016, **61(8)**: 1-18.

[44] Wang WM, Wang WD, Liu YM*, et al.* Synergistic improvement of flexural strength and fracture toughness in Si_3N_4 ceramics featuring high-entropy grain boundary phase. *J Adv Ceram*. 2026, **15(2)**: 9221230.

[45] Gao W, Wang XG, Wang XF*, et al.* Preparation of (Ti,Zr,Hf)B_2 powders and effect of B_4C content on the high temperature flexural strength of medium entropy ceramics. *J Adv Ceram*. 2023, **44(4)**: 342-351.

[46] Xuan WP, Ji YC, Liu BS*, et al.* Spark plasma sintering of boron nitride micron

tubes reinforced boron carbide ceramics with excellent mechanical property. *Int J Appl Ceram Technol*. 2023, **20(3)**: 1457-1469.

[47] Demirskyi D, Vasylkiv O. Analysis of the high-temperature flexural strength behavior of B_4C–TaB_2 eutectic composites produced by in situ spark plasma sintering. *MSEA*. 2017, **697**: 71-78.

[48] Yue XY, Huo MD, Liu JQ*, et al.* Microstructure and properties of bilayered B_4C-based ceramics. *J Eur Ceram Soc*. 2022, **42(8)**: 3404-3414.

[49] So SM, Choi WH, Kim KH*, et al.* Mechanical properties of B_4C–SiC composites fabricated by hot-press sintering. *Ceram Int*. 2020, **46(7)**: 9575-9581.

[50] Ka JH, Kim KH, Choi W*, et al.* Improving the Fracture Toughness of Boron Carbide via Minor Additions of SiC and TiB_2 Through Hot-Press Sintering. *Mat.* 2024, **17(24)**: 6233.

[51] Song Q, Zhang ZH, Hu ZY*, et al.* Microstructure and mechanical properties of super-hard B4C ceramic fabricated by spark plasma sintering with (Ti_3SiC_2+Si) as sintering aid. *Ceram Int*. 2019, **45(7, Part A)**: 8790-8797.

[52] Yan X, Zhou X, Wang H. Effect of Additive Ti_3SiC_2 Content on the Mechanical Properties of B_4C–TiB_2 Composites Ceramics Sintered by Spark Plasma Sintering. *Mat.* 2020, **13(20)**: 4616.

[53] Fan L, Song XW, Zhao PF*, et al.* Super strong B_4C ceramics prepared by dynamic sinter forging. *J Eur Ceram Soc*. 2023, **43(9)**: 4209-4214.

[54] Belon R, Antou G, Pradeilles N*, et al.* Mechanical behaviour at high temperature

of spark plasma sintered boron carbide ceramics. *Ceram Int*. 2017, **43(8)**: 6631-6635.

[55] Chen XZ, Li YH, Qi YJ*, et al.* Preparation of Si_3N_4 ceramics with high thermal conductivity and mechanical properties using novel $Gd_3Si_2C_2$ as a sintering aid. *Ceram Int*. 2025, **51(8)**: 9931-9938.

[56] Chen XZ, Li YH, Liu YW*, et al.* Effect of $Gd_3Si_2C_2$ content and sintering time on the microstructure and thermal conductivity of Si_3N_4 ceramics. *Ceram Int*. 2025, **51(27, Part A)**: 51830-51838.

[57] Liu YK, Liu YG, Yu HJ*, et al.* Enhanced luminescence efficiency and thermal stability via introduction of non-rare earth Bi^{3+} in $Gd_5Si_2BO_{13}:Eu^{3+}$. *J.Rare Earths*. 2023, **41(7)**: 989-996.

[58] Yuan JL, Zhang ZJ, Wang XJ*, et al.* Synthesis and VUV–UV spectroscopic properties of rare earth borosilicate oxyapatite: $RE_5Si_2BO_{13}:Ln^{3+}$ (RE=La, Gd, Y; Ln=Eu, Tb). *Solid State Chem*. 2007, **180(4)**: 1365-1371.

[59] Makrovets LA. Y_2O_3–SiO_2 Phase Diagram. *Russ Metall*. 2023, **2023(8)**: 1155-1158.